



# Synthesis of Size-Controllable NiCo<sub>2</sub>S<sub>4</sub> Hollow Nanospheres Toward Enhanced Electrochemical Performance

Lei Zhang, Haitao Zhang\*, Xiang Chu, Fangyan Liu, Chunsheng Guo\*, and Weiqing Yang\*

Although the synthesis of novel nanostructured metal sulfides has been well established, further size-controllable optimization is still valuable to enhance their performance for various applications. Herein, a self-template method to size-controllably synthesize the hollow NiCo<sub>2</sub>S<sub>4</sub> nanospheres is reported. Uniformly monodisperse NiCo precursors with diameter widely ranging from 97 to 550 nm are controllably synthesized and subsequently transformed into hollow NiCo<sub>2</sub>S<sub>4</sub> nanospheres through in situ sulfidation. Smaller nanoparticles' diameter results in the hollow NiCo<sub>2</sub>S<sub>4</sub> nanospheres larger surface area and thinner shell thickness and hence provides much more electrochemical active sites as well as facilitate the ion and electron transfer. Consequently, the hollow NiCo<sub>2</sub>S<sub>4</sub> nanospheres—used as the electrode materials in supercapacitors—achieve 19% enhancement of specific capacity from 484.8 to 575.1 C g<sup>-1</sup> through lowering the 42.5% diameter of hollow NiCo<sub>2</sub>S<sub>4</sub> nanospheres from 407 to 234 nm. Moreover, the hollow NiCo<sub>2</sub>S<sub>4</sub> nanospheres with 234 nm diameter exhibit superior rate capacity indicated by 49% capacity retention from 1 to 50 A g<sup>-1</sup> and excellent cycling stability (77% after 2000 cycles). Furthermore, this method is a potentially general strategy in the size-controllable synthesis of the metal sulfides hollow nanostructures and results in the remarkable electrochemical applications.

## 1. Introduction

Metal sulfides intrinsically possess better conductivity and higher electrochemical activity than their corresponding metal oxides,<sup>[1]</sup> representing a unique class of valuable electrode materials for electrochemical storage and conversion systems<sup>[2–4]</sup> including supercapacitors,<sup>[5–7]</sup> lithium-ion batteries,<sup>[8–11]</sup> sodium-ion batteries,<sup>[12–17]</sup> and water-splitting.<sup>[18–20]</sup> Compared with the monometal sulfides, mixed metal sulfides (MMSs) further present much more abundant redox reactions and higher electroconductibility with remarkably enhanced electrochemical performance. On the other hand, their uniquely micro/nano-architected hollow structures can effectively enlarge the surface area, lower density, and present high pore volume that differs from their solid counterparts. Therefore, many research works have been devoted to the rational design and synthesis of hollow MMS micro/nanostructure materials.

Up to the present, a variety of synthetic methods have been reported to prepare MMSs.

Among them, template methods—including hard template methods, soft template methods, and self-template methods—have been viewed as the most common synthetic strategies. Furthermore, featured as low-temperature and energy-saving, solution-based methods have been demonstrated to be highly effective and versatile to achieve high-quality uniform MMS hollow micro/nanostructures. For example, Zhang et al.<sup>[21]</sup> synthesized hierarchical MoS<sub>2</sub> microboxes made of ultrathin nanosheets by a MnCO<sub>3</sub> hard templating assisted hydrothermal strategy. Chen designed uniform one-dimensional M<sub>x</sub>Co<sub>3–x</sub>S<sub>4</sub> hollow tubular using polymeric nanofibers as a soft templating.<sup>[22]</sup> However, the hard and soft template methods are always limited due to the lack of available templates, the vulnerability from both acid and thermal treatment, and the incompatibility between MMSs and template materials.<sup>[23]</sup> It was suggested that more synthesis of the MMSs prefers the self-template methods for their powerful and versatile features. Many hollow MMS micro/nanostructures have extensive coverage, for instance, nano-frames,<sup>[24]</sup> microboxes,<sup>[25]</sup> nanoprisms,<sup>[26]</sup> some microstructures with complex interior,<sup>[27]</sup> etc. Despite that, previous works mainly focus on the different morphologies or various composition, while only a few reports demonstrate further size optimization for those hollow nanostructures to achieve better performance.

This paper proposes a potentially general strategy based on a self-template method to synthesize size-controllable nickel-cobalt sulfide (NiCo<sub>2</sub>S<sub>4</sub>) hollow nanospheres. The synthesis has a two-step

Dr. L. Zhang, Dr. H. Zhang, X. Chu, Dr. F. Liu  
Key Laboratory of Advanced Technologies of Materials (Ministry of Education), School of Materials Science and Engineering, Southwest Jiaotong University, Chengdu 610031, China  
E-mail: haitaozhang@swjtu.edu.cn

Prof. C. Guo  
School of Physic Science & Technology, Superconductivity and New Energy R&D Center, Southwest Jiaotong University, Chengdu Sichuan 610031, China  
E-mail: csguo@swjtu.edu.cn

Prof. W. Yang  
Key Laboratory of Advanced Technologies of Materials (Ministry of Education), School of Materials Science and Engineering, Southwest Jiaotong University, Chengdu 610031, China  
E-mail: wqyang@swjtu.edu.cn

State Key Laboratory of Traction Power, Southwest Jiaotong University, Chengdu 610031, China  
E-mail: wqyang@swjtu.edu.cn

The ORCID identification number(s) for the author(s) of this article can be found under <https://doi.org/10.1002/eem2.12113>.

DOI: 10.1002/eem2.12113

solvothermal process: first surfactant-assisted (polyvinyl pyrrolidone, PVP) process to synthesis monodisperse NiCo precursor (denoted as NC-pres) solid nanospheres, and subsequent in situ sulfidation process (called anion exchange process<sup>[27]</sup>) to form NiCo<sub>2</sub>S<sub>4</sub> hollow nanospheres. With this method, the additive PVP mass can tunably synthesize NC-pres nanospheres with the different diameter ranging from 97 to 550 nm, which can be sulfurized to hollow NiCo<sub>2</sub>S<sub>4</sub> nanospheres. Used as electrode materials for electrochemical supercapacitors, the hollow NiCo<sub>2</sub>S<sub>4</sub> nanospheres—with increased surface areas and thinner shell thickness—provide more electrochemical active sites, shortened ion/electron path, and more remarkable electrochemical performance.

## 2. Results and Discussions

### 2.1. Formation of Size-Controllable NiCo<sub>2</sub>S<sub>4</sub> Hollow Nanospheres

Because of the mechanism of the self-template method, the NiCo precursors (NC-pres) are vital to prepare size-controllable NiCo<sub>2</sub>S<sub>4</sub> hollow nanospheres. The Scheme I illustrates the synthesis strategy for different-diameter NC-pres (see Section 4 for details). A PVP-assisted solvothermal procedure was first employed to obtain highly uniform and monodisperse NC-pres solid spheres participated with nickel nitrate, cobalt nitrate, and glycerol in isopropanol solution. Subsequently, the as-prepared NC-pres were dispersed in thioacetamide (TAA) ethanol solution, and sulfurized via the anion exchange process to hollow NiCo<sub>2</sub>S<sub>4</sub> nanospheres (Scheme II).<sup>[6,26,28]</sup> Specifically, sulfide ions—originated from the hydrolyzation of TAA—react with nickel and cobalt ions at high temperature first to form a NiCo<sub>2</sub>S<sub>4</sub> thin layer on the surface of NC-pres nanospheres. The further reaction of relatively diffusive metal and sulfide ions through this layer will dissipate the inner NC-pres core and convert solid NC-pres to hollow NiCo<sub>2</sub>S<sub>4</sub> spheres (Figure S1). Finally, the thermal annealing process was applied at 450 °C, 4 h in Ar atmosphere to improve the crystallinity.

To facilitate the description, we term the different-diameter NiCo precursors and resultant NiCo<sub>2</sub>S<sub>4</sub> as P<sub>n</sub> and S<sub>n</sub>, where n denotes the weight of additive PVP (n = 0, 15, 50, 150, 200, 300, and 500 mg in this experiment). The field-emission scanning electron microscopy (FESEM) examines the morphology of NC-pres. In the panoramic FESEM images (Figure 1a), highly uniform and monodisperse nanospheres compose these NC-pres without any impurities. In the magnified FESEM images (Figure 1b,c), each NC-pres nanosphere has a rather smooth surface over the whole particle. Also, the average diameter from P<sub>0</sub> to P<sub>500</sub> is observed to be 550, 407, 307, 234, 148, 110, and 97 nm (Figure S2d), and the corresponding exponential relationship between the NC-pres' diameter with the additive PVP mass is deduced as follow:

$$y = 77.3 + 328.1 \times e^{\frac{-x}{61.3}} + 149.1 \times e^{\frac{-x}{10.3}} \quad (1)$$

where x is the additive PVP mass, and y is the diameter of NC-pres nanospheres. The unique size-induced physical deposition phenomena in aqueous solution further confirm the synthesis of different-diameter NC-pres (Figure S2a–c). Transmission electron microscopy (TEM) images of the representational P<sub>500</sub> sample present uniform contrast, clearly indicates their inner solid and dense nature (Figure S3a,b). However, the X-ray diffraction (XRD) pattern shows no prominent diffraction peak (Figure S3c), which implies the poor crystallinity.

To investigate the roles of PVP in detail, we conduct thermogravimetric analysis (TGA) (Figure S4c). The TGA curve shows a similar weight loss of about 48.5% at 450 °C in the different-diameter nanospheres, suggesting the composition of all the samples is uniform and proportional. Also, the sintering temperature is higher than the previously reported value (300 °C) for the NiCo-glycerate (without additive PVP),<sup>[29]</sup> which reveals that PVP can coordinate with the metal ion (Co<sup>2+</sup>, Ni<sup>2+</sup>) and prevent thermal decomposition. The Fourier transform infrared spectroscopy confirms the formation of PVP-coordinated NC-pres (Figure S4d). Besides, another experiment has been carried out by adding excessive polyvinyl alcohol (model number: 1799). The resultants receive a limitedly reduced diameter (~320 nm) but inconsistent morphology (Figure S4a,b). Thus, we hypothesis the PVP plays triple roles in this process, which should be that controls the nucleation rate through raising solution viscosity, be involved in the NC-pres as ligand molecule, and maintains uniform morphology as a surfactant.

### 2.2. Characterizations of Size-Controllable NiCo<sub>2</sub>S<sub>4</sub> Hollow Nanospheres

After the same sulfidation treatment in the TAA solution, the as-synthesized NiCo<sub>2</sub>S<sub>4</sub> well inherits the original grain diameter from corresponding NC-pres. The FESEM images (Figure 2) show that the surface of these samples is much rough, porous, and composed of compactly packed nanoparticles. With the reduced diameter of NiCo<sub>2</sub>S<sub>4</sub> nanospheres, the shell seems to suffer unsatisfactory mechanical performance. We can observe the hollow interior from some broken nanospheres. Moreover, more fragments can be found in S500 nanosphere samples (Figure S5).

Transmission electron microscopy study presents the hollow interior and detailed geometrical structure of the as-formed nanospheres. Figure 3a–d exhibits a sharp contrast of NiCo<sub>2</sub>S<sub>4</sub> nanospheres between the center and the edge. Distinguishing from the S15, S50, and S150 samples, with a diameter beyond 500 nm, the NC-pres nanospheres are prone to experiencing a secondary anion exchanging process in the inner core and receiving the core-shell structure (S0 sample, Figure 3a).<sup>[27]</sup> Many mesopores distribute on the shell of the nanospheres, which may ascribe to the ion diffusion process and the PVP decomposition during the crystal transformation process. The thickness of the shell presents a gradually decreasing trend that ~42 nm (S0), 20 nm (S15), 15 nm (S50), and 8 nm (S150), which may result from the less interior metal ion source converted to NiCo<sub>2</sub>S<sub>4</sub> shell in a small diameter nanosphere. That may simultaneously reason for the reduced mechanical property. The TEM images of S200, S300, and S500 are presented in Figure S6, which is consistent with the FESEM results.

Energy-dispersive X-ray spectrum (EDS) elemental mapping and composition analysis of representational S50 sample (Figure 3e,f) demonstrate the uniform distribution of the Ni, Co, and S elements. The interplanar spacing of the counterpart is observed to be 0.54 nm in the high-resolution transmission electron microscopy (HRTEM) image, as shown in Figure 3g, which is in good agreement with the (111) lattice planes of NiCo<sub>2</sub>S<sub>4</sub> phase. The selected area electron diffraction (SAED) pattern (Figure 3h) implies the polycrystalline property with the diffraction rings assigned to the 440, 444, and 800 planes of the cubic NiCo<sub>2</sub>S<sub>4</sub> phase.

The N<sub>2</sub> adsorption–desorption measurements show increasing Brunauer–Emmett–Teller-specific surface areas, namely 24.5 (S0), 46.5 (S15), 51.3 (S150), and 58.6 (S500) m<sup>2</sup> g<sup>-1</sup> (Figure 4a and

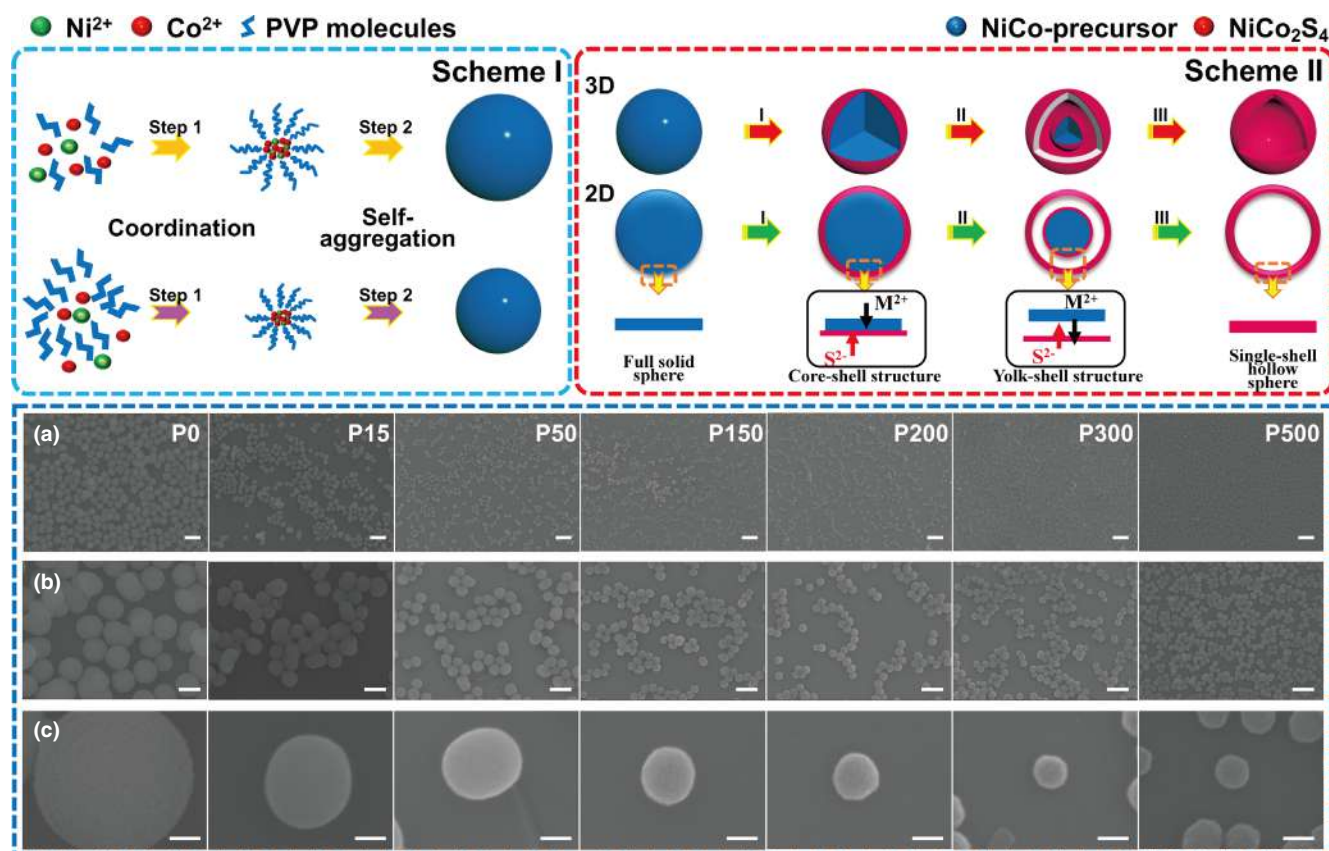


**Figure 1.** The synthesis of size-controllable  $\text{NiCo}_2\text{S}_4$  hollow nanospheres. Scheme I Schematic illustration of the PVP-assisted size-controllable synthesis of nickel-cobalt precursors, and Scheme II shows the formation process of final  $\text{NiCo}_2\text{S}_4$  hollow nanospheres. The SEM images of NiCo precursors with different additive PVP mass with scale bar a) 1  $\mu\text{m}$ , b) 500 nm, and c) 100 nm.

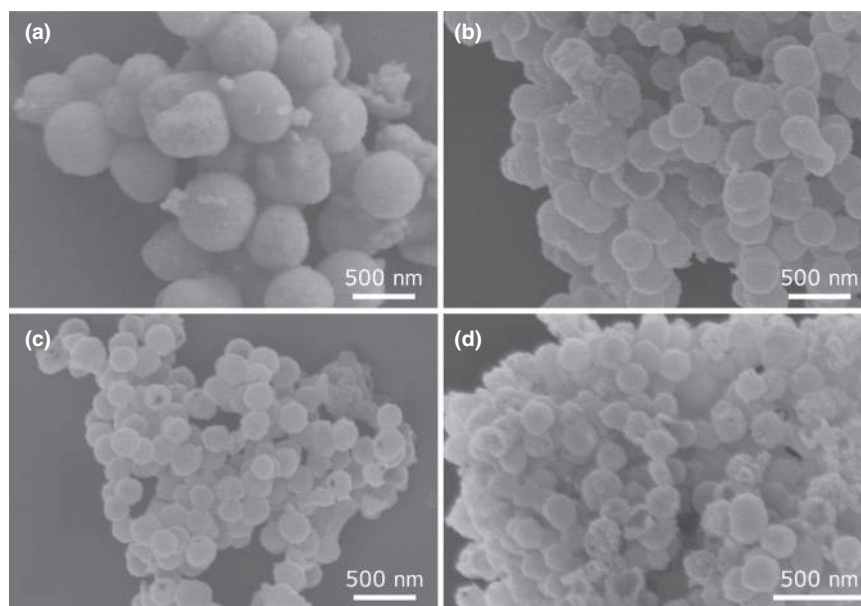


**Figure 2.** The SEM images of different-diameter  $\text{NiCo}_2\text{S}_4$  nanosphere samples under the same sulfidation treatment: a) S0, b) S15, c) S50, and d) S150 with the same scale bar: 500 nm.

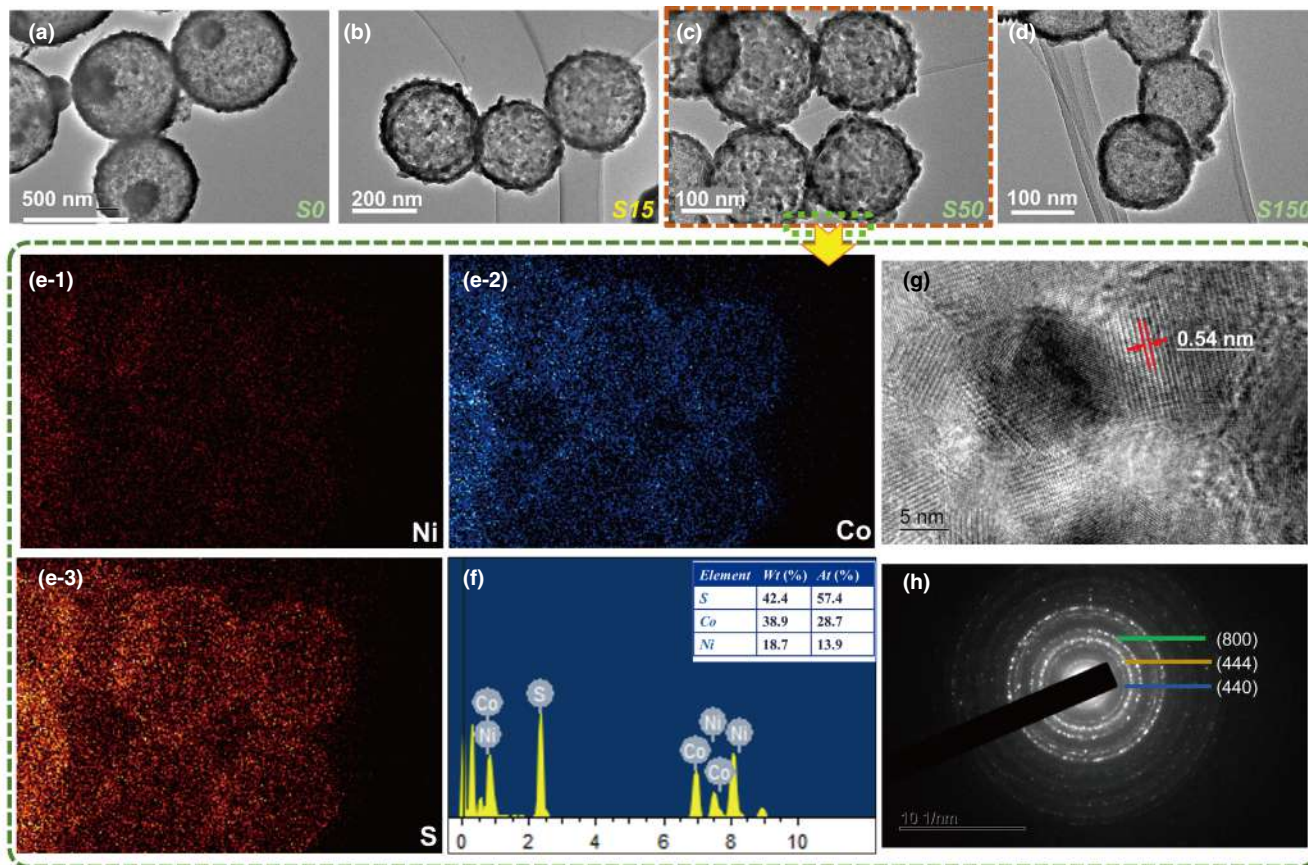


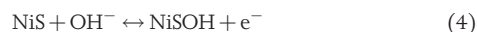
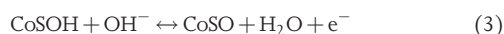
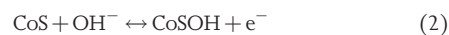
**Figure 3.** The TEM images of different-diameter  $\text{NiCo}_2\text{S}_4$  nanospheres: a) S0, b) S15, c) S50, and d) S150. e,f) The EDX-elemental mapping images and elemental composition analysis from TEM of the S50 sample. g,h) Corresponding HRTEM image and SAED patterns image.

detailed in Figure S7). The larger specific surface area will endow the  $\text{NiCo}_2\text{S}_4$  nanospheres with more electrochemically active sites. The XRD patterns depicted in Figure 4b were utilized to characterize the phase purity and crystallinity of the  $\text{NiCo}_2\text{S}_4$  (S50). The main diffraction peaks can be indexed and assign to cubic  $\text{NiCo}_2\text{S}_4$  (JCPDS card 20-0782), the corresponding crystal structure model insets the inside. Surprisingly, two impurity peaks were detected around  $30^\circ$  and  $52^\circ$ , which assigns to  $\text{Co}_9\text{S}_8$ . This result may attribute to a bit over sulfidation-induced decomposition in the hydrothermal process.<sup>[28,30]</sup>

We further conduct the X-ray photoelectron spectroscopy to investigate the chemical composition. Figure S8 shows the full survey spectra of the S0, S50, and S150 samples with all peaks marked. The Gaussian fitting method fits the Co 2p, Ni 2p, and S 2p spectra, considered with two spin-orbit doublets and two shake-up satellites (marked "Sat.") (Figure 4c–e). Concretely, the Ni 2p—concluding  $2p_{3/2}$  and  $2p_{1/2}$ —displays the atoms located at 853.9 eV ( $\text{Ni}^{2+}$ ), 855.3 eV ( $\text{Ni}^{3+}$ ), and 872.9 eV ( $\text{Ni}^{2+}$ ), 879.3 eV ( $\text{Ni}^{3+}$ ); the Co 2p—concluding  $2p_{3/2}$  and  $2p_{1/2}$ —peaks at 778.6 eV ( $\text{Co}^{3+}$ ), 780.7 eV ( $\text{Co}^{2+}$ ), and 793.6 eV ( $\text{Co}^{3+}$ ), 796.8 eV ( $\text{Co}^{2+}$ ); and the S 2p at 161.8 eV ( $2p_{3/2}$ ) and 162.4 eV ( $2p_{1/2}$ ). The intensity information reflects another significant trend that the nickel and cobalt ions in the reduced diameter nanospheres present a higher valence state at  $\text{Ni}^{3+}$  and  $\text{Co}^{3+}$  than  $\text{Ni}^{2+}$  and  $\text{Co}^{2+}$ .

### 2.3. Electrochemical Characterizations of Size-Controlable $\text{NiCo}_2\text{S}_4$ Hollow Nanosphere Electrodes

The electrochemical performance of the different-diameter  $\text{NiCo}_2\text{S}_4$  hollow nanospheres is investigated in the three-electrode system with a KOH aqueous electrolyte. The cyclic voltammetry (CV) curves of the S0, S15, S50, and S150 samples, presented in Figure S9, were measured at different scan rates ranging from 2 to  $100 \text{ mV s}^{-1}$  with a potential window from  $-0.1$  to  $0.55 \text{ V}$ . Figure 5a shows the characteristic CV curves at a constant scan rate of  $5 \text{ mV s}^{-1}$ . All the CV curves contain two pairs of symmetric redox peaks and reveal the reversibility of the as-fabricated hollow  $\text{NiCo}_2\text{S}_4$  nanospheres. The mechanism of the electrochemical reactions may be explained by the reversible faradaic redox processes of  $\text{Co}^{2+}/\text{Co}^{3+}/\text{Co}^{4+}$  and  $\text{Ni}^{2+}/\text{Ni}^{3+}$  in KOH solution<sup>[23,31,32]</sup>:



The reversible redox reactions result in the formation of NiSOH and CoSOH. A main pair of redox peaks and voltage separation about  $0.8 \text{ V}$

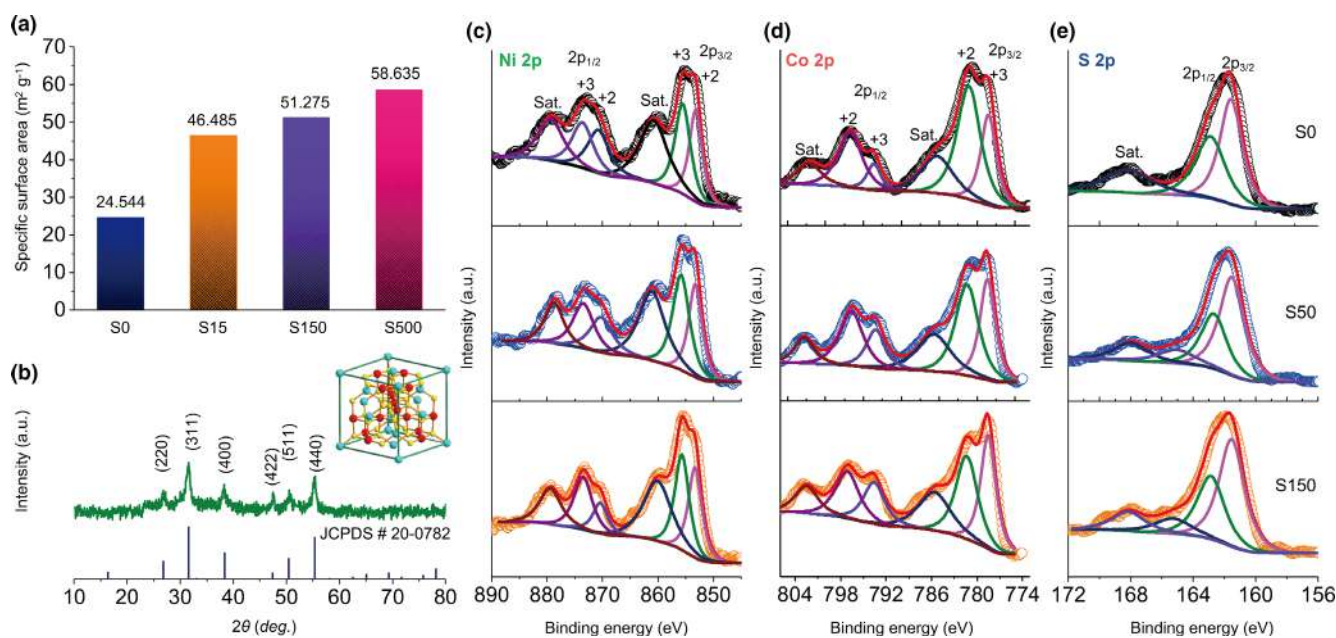


**Figure 4.** a) The BET-specific surface area result of different-diameter NiCo<sub>2</sub>S<sub>4</sub> nanospheres: S0, S50, S150, and S500; b) XRD pattern of NiCo<sub>2</sub>S<sub>4</sub> S50 nanospheres sample. c–e) The high-resolution XPS comparison of S0, S50, and S150 samples.

between the oxidation and reduction peak can be observed clearly, which indicates the battery-type property. The overlapping oxidation peaks around 0.33 V originate from the process of NiS to NiSOH and CoSOH to CoSO. The overlapping reduction peaks around 0.23 V result from the reverse process. Moreover, compared with the S0 and S15 samples, the S50 and S150 samples show a smaller voltage difference between the anodic and cathodic peaks, indicating much more reversible capacity.

Figure S10 presents the galvanostatic charge/discharge (GCD) curves of the S0, S15, S50, and S150 samples at a different current density ranging from 1 to 50 A g<sup>-1</sup>, and Figure 5b shows the representative GCD curves at the current density of 2 A g<sup>-1</sup>. Consistent with the CV curves, the voltage plateaus in the charging/discharging curves reveal the presence of some Faradaic processes. The specific capacity of size-controllable NiCo<sub>2</sub>S<sub>4</sub> hollow nanospheres electrodes is calculated by the formula,

$$C = (I\Delta t)/m \quad (5)$$

where  $I$  is the discharge current,  $\Delta t$  is the discharge time, and  $m$  is the mass of the electrode material. Figure 5c plots the specific capacity as a function of different current density. At a current density of 1 A g<sup>-1</sup>, the specific capacity of S0, S15, S50, and S150 is 500, 484.8, 543.7, and 575.1 C g<sup>-1</sup>. The S0 sample presents a little higher performance than S15, which may occur due to the core-shell nanostructure merits, as reported previously.<sup>[25]</sup> Compared with the S15 sample, the S150 exhibits a capacity increase in around 19% with a 42.5% diameter decrease from 407 to 234 nm. At a high current density of 50 A g<sup>-1</sup>, the capacity of the S15, S50, and S150 samples remains 395, 525, and 570 C g<sup>-1</sup>, corresponding to about 40.7%, 48.2%, and 49.5% of the capacity at 1 A g<sup>-1</sup>, presenting the excellent rate capability. The thinner

shell mentioned above can significantly reduce the path for promoting ion and electron diffusion in the electrochemical system.<sup>[18,33,34]</sup> The electrochemical impedance spectrum of different-diameter NiCo<sub>2</sub>S<sub>4</sub> hollow nanosphere electrodes is plotted in Figure S11. The smaller diameter of nanospheres will result in the smaller resistance and more significant slope, which consolidates the faster ion and electron transfer rate in the charge/discharge process and better rate capability. Despite that, the S300 and S500 (Figures S12 and S13) nanosphere electrodes present a little bit of performance degradation with a specific capacity of 548.9 and 506 C g<sup>-1</sup> (@ 1 A g<sup>-1</sup>). That may stem from the morphological destruction as observed in FESEM and TEM images.

The cycling performance—as another critical factor for the energy storage device—is evaluated by repeated charge/discharge test at a current density of 5 A g<sup>-1</sup>. With the diameter of the S0, S15, S50, and S150 nanosphere samples reduced from 550 to 234 nm, 48.1%, 41.7%, 62.5%, and 77% of the initial specific capacity remain after 2000 cycles. As a result, the reduced diameter NiCo<sub>2</sub>S<sub>4</sub> nanospheres synthesized by adding PVP surfactant can effectively improve the electrochemical performance.

It is noted that the size-controllable synthesis of NiCo<sub>2</sub>S<sub>4</sub> hollow nanospheres as electrochemical supercapacitor electrode is only a proof-of-concept work. It paves a way to tailor electrochemical performance through designing different size micro/nanostructure for hollow metal sulfide electrodes. On the one hand, many MMS composition and nanostructure have been prepared and receive excellent performance based on a similar self-template method. On the other hand, hollow MMS materials with lower density, larger surface area, and higher capacity can be designed to allow for various applications. Thus, the size-controllable synthesis of hollow MMS materials will have a profound impact in the areas of energy storage and conversion.

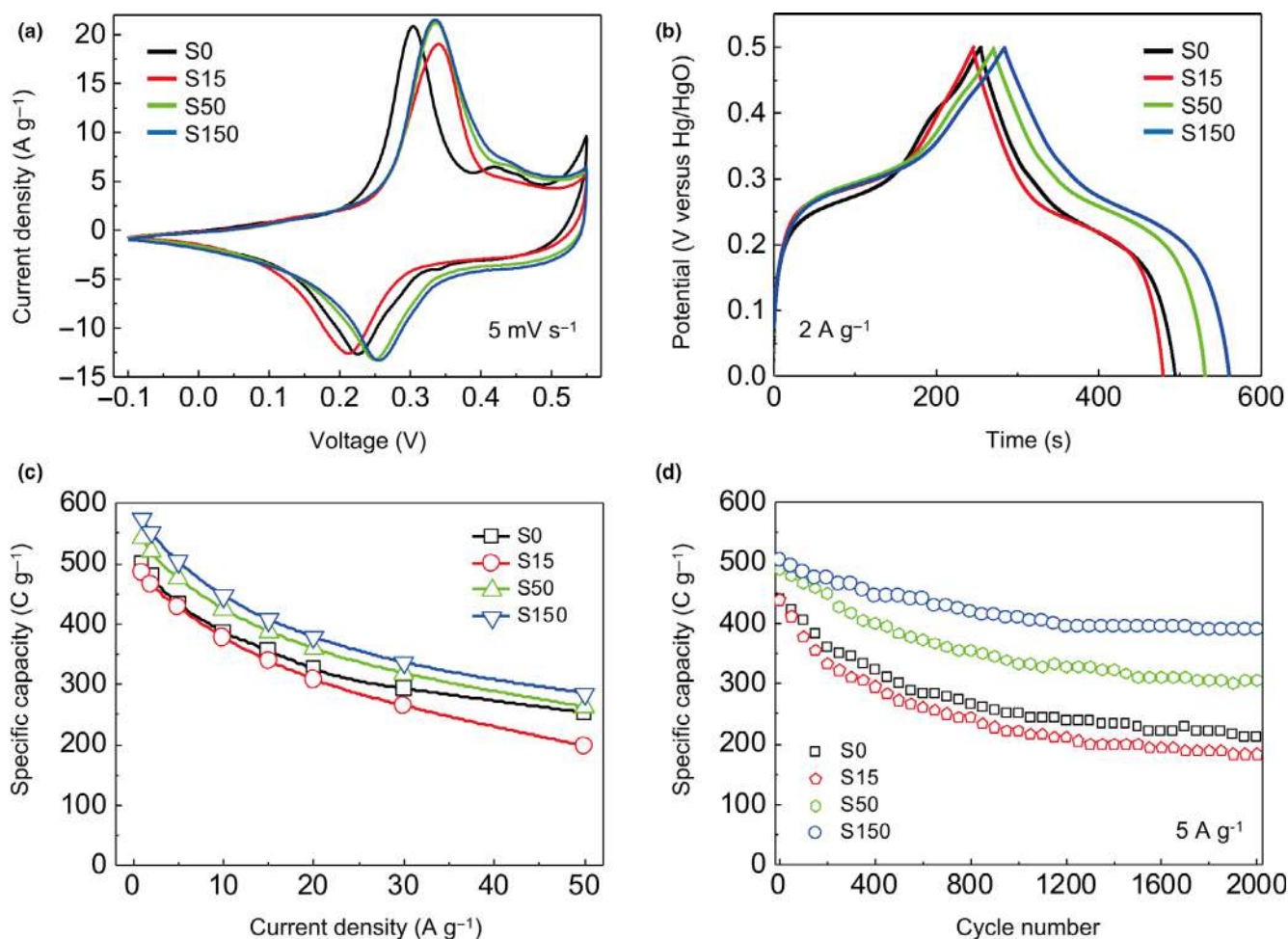


**Figure 5.** a) The CV curves and b) GCD curves of the NiCo<sub>2</sub>S<sub>4</sub> S0, S15, S50, S150 nanospheres measured at a scan rate of 5 mV s<sup>-1</sup> and a current density of 2 A g<sup>-1</sup>. c) Corresponding plot of the specific capacity as a function of scan rate and d) cycling performance at a 5 A g<sup>-1</sup>. The reference electrode is a saturated calomel electrode.

### 3. Conclusion

In summary, we report a new method based on a two-step hydrothermal process to size-controllably synthesis NiCo<sub>2</sub>S<sub>4</sub> nanospheres for electrochemical energy storage. The different PVP masses were added as a surfactant to obtain different sized nickel-cobalt precursor nanospheres. Followed by the anion exchange process, the different size hollow NiCo<sub>2</sub>S<sub>4</sub> nanospheres were synthesized with a diameter of 550, 407, 307, 234, 148, 110, and 97 nm. The reduced diameter of hollow NiCo<sub>2</sub>S<sub>4</sub> nanospheres promotes the larger specific surface area and thinner shell thickness, which endows much more electrochemical sites and shortened ion and electron path. Specifically, the S150 NiCo<sub>2</sub>S<sub>4</sub> electrode presents a superior specific capacity of 575.1 C g<sup>-1</sup> at the current density of 1 A g<sup>-1</sup>, great rate capacity of 49.5% remained from 1 to 50 A g<sup>-1</sup>, and long cycling stability (77% after 2000 cycles). This work not only provides a potentially general size-controllable synthesis method of NiCo<sub>2</sub>S<sub>4</sub> hollow nanostructures but also promotes the prosperous development of the area of energy storage and conversion.

Nevertheless, our current work shows many capacities yet still has many aspects that can be improved on. First, the optimal sulfidation

process should be explored. Because previous works have been demonstrated, complex nanostructures such as core-shell structure, ball in ball structure, and multiple-shell structure present better rate performance and cycling stability.<sup>[35-37]</sup> The sulfidation temperature and time also should be investigated for different size nanospheres, which will make a big difference to mechanical performance, chemical valence state, and surface appearance of nanomaterial.<sup>[32,33]</sup> That is vital to achieving higher electrochemical performance. Last, these different size electrode materials should be tried in various applications of energy storage and energy for a better effect.

### 4. Experimental Section

**Synthesis of Nickel-Cobalt Precursor Nanospheres with Different Diameter:** All the reagents were directly used without further treatment. Two steps were involved in the process to prepare size-controllable NiCo<sub>2</sub>S<sub>4</sub> nanospheres. First, during a typical hydrothermal procedure, different PVP masses (0, 15, 50, 150, 200, 300, 500 mg) (Kelong Chemical Reagent Corporation, Chengdu, China) were dissolved in 40 mL isopropanol and 8 mL glycerol, forming a transparent solution. Subsequently, 0.125 mmol of Ni(NO<sub>3</sub>)<sub>2</sub>•6H<sub>2</sub>O (Aladdin Industrial

Corporation, Shanghai, China) and 0.125 mmol of  $\text{Co}(\text{NO}_3)_2 \cdot 6\text{H}_2\text{O}$  (Aladdin Industrial Corporation) were added into the above-mentioned solution. In this process, a clear pink solution was obtained after stirring for 20 min and then poured into a 100 mL Teflon-lined stainless-steel autoclave with a fixed heating temperature of 180 °C for 6 h. After naturally cooling to ambient temperature, the brown precipitates were collected by centrifugation, washed several times with ethanol, and dried in an oven at 85 °C.

**Synthesis of Size-Controllable  $\text{NiCo}_2\text{S}_4$  Hollow Nanospheres:** To synthesis size-controllable  $\text{NiCo}_2\text{S}_4$  hollow nanospheres, 30 mg prepared NiCo precursors and 50 mg thioacetamide (Aladdin Industrial Corporation) were dispersed into 20 mL ethanol by ultrasonic. Then, the above mixture was transferred into a 50 mL autoclave and heated at a fixed temperature of 160 °C for 6 h. The  $\text{NiCo}_2\text{S}_4$  hollow nanospheres were received after the second centrifugation collection and several times washing with ethanol. Last, to improve the crystallinity, the product was annealed at 450 °C (2 °C  $\text{min}^{-1}$  ramp) for 4 h with Ar atmosphere.

**Material Characterizations:** The morphology and structure were characterized using field-emission scanning electron microscopy (FESEM) (JEOL, JSM-7001F). Samples dispersed onto silicon substrate for FESEM characterizations. Transmission electron microscopy and high-resolution TEM characterizations were performed with a JEOL JEM-2100F operating at an accelerating voltage of 200 kV. Energy-dispersive spectrometer (EDS)—attached on JEM-2100F—acquires elemental mapping and composition analysis. X'Pert Pro MPD (Holland) X-ray diffraction performs the X-ray diffraction patterns between 10 and 80° with Cu  $\text{K}\alpha_1$  radiation ( $\lambda = 0.154$  nm). Kratos XSAM800 spectroscopy performs the X-ray photoelectron spectroscopy characterizations. Micro-meristics ASAP 2020 surface area and pore size analyzer measure the Brunauer–Emmert–Teller surface areas and density functional theory pore size distribution of different-diameter  $\text{NiCo}_2\text{S}_4$  hollow nanospheres by  $\text{N}_2$  adsorption–desorption isotherm at  $-196$  °C. Fourier transform infrared (FTIR) spectroscopy was performed between 400 and 4000  $\text{cm}^{-1}$  using a Nicolet 5700 FTIR spectrometer. Thermogravimetric analysis (NETZSH, STA 449C) was carried out with a 10 °C  $\text{min}^{-1}$  temperature ramp under an  $\text{N}_2$  atmosphere.

**Electrochemical Measurements:** For electrochemical characterizations, the measuring electrodes were prepared by mixing the electroactive material, acetylene black, and polyfluorotetraethylene (PTFE) binder with a weight ratio of 85:8:7 in isopropyl alcohol, and blended for 30 min before using. Then, drip the as-mixed slurry onto Ni foam (about 500  $\mu\text{m}$  thickness) with a loading area of 1  $\text{cm}^2$ . Meantime, the loading mass (about 1.5 mg) of materials in each electrode was controlled carefully based on the Mettler Toledo MS105DU electronic balance with the precision of 0.01 mg. Last, the as-prepared nickel foam was rolled down to 100- to 120- $\mu\text{m}$ -thick films and dried at 85 °C for 12 h to remove excess isopropanol. Subsequently, the CHI660E electrochemical workstation (Shanghai Chenhua Instrument Co. Shanghai, China) performs electrochemical measurements with a 6.0 M aqueous KOH electrolyte in a three-electrode configuration where a Pt foil with 3  $\text{cm} \times 2$   $\text{cm}$  area served as the counter electrode and a Hg/HgO electrode as the reference electrode. The LAND battery test system measures the cycling performance by chronopotentiometry technique.

## Acknowledgements

L.Z., H.Z. contributed equally to this work. The research is supported by the National Natural Science Foundation of China (No. 51602265), the Special Funding of China Postdoctoral Science Foundation (No. 2018T110992), and the Sichuan Science and Technology Program (No. 2018RZ0074).

## Conflict of Interest

The authors declare no conflict of interest.

## Supporting Information

Supporting Information is available from the Wiley Online Library or from the author.

## Keywords

nickel–cobalt sulfides, self-template method, size-controllable, supercapacitor

Received: May 12, 2020

Revised: May 28, 2020

- [1] W. Yang, Z. Gao, J. Ma, X. Zhang, J. Wang, J. Liu, *J. Mater. Chem. A* **2014**, *2*, 1448.
- [2] N. Zhang, J. Chen, Y. Huang, W. Guo, J. Yang, J. Du, X. Fan, C. Tao, *Adv. Mater.* **2016**, *28*, 263.
- [3] J. Chen, Y. Huang, N. Zhang, H. Zou, R. Liu, C. Tao, X. Fan, Z. L. Wang, *Nat. Energy* **2016**, *1*, 16138.
- [4] Z. Chai, N. Zhang, P. Sun, Y. Huang, W. Mai, *ACS Nano* **2016**, *10*, 9201.
- [5] Y. Tao, L. Ruiyi, Z. Lin, M. Chenyang, L. Zaijun, *Electrochim. Acta* **2015**, *176*, 1153.
- [6] L. Zhang, H. Zhang, L. Jin, B. Zhang, F. Liu, H. Su, F. Chun, Q. Li, J. Peng, W. Yang, *RSC Adv.* **2016**, *6*, 50209.
- [7] W. Xie, Y. Song, S. Li, M. Shao, M. Wei, *Energy Environ. Mater.* **2019**, *2*, 158.
- [8] Y. Lu, L. Yu, X. W. Lou, *Chem.* **2018**, *4*, 972.
- [9] Y. Wu, X. Huang, L. Huang, J. Chen, *Energy Environ. Mater.* **2019**, <https://doi.org/10.1002/eem2.12088>
- [10] C. Zhang, Y. Ma, X. Zhang, S. Abdolhosseinzadeh, H. Sheng, W. Lan, A. Pakdel, J. Heier, F. Nüesch, *Energy Environ. Mater.* **2020**, *3*, 29.
- [11] C. Han, H. Li, R. Shi, L. Xu, J. Li, F. Kang, B. Li, *Energy Environ. Mater.* **2018**, *1*, 75.
- [12] X.-W. Lou, *Angew. Chem. Int. Ed. Engl.* **2019**, *58*, 1.
- [13] X. Wang, Y. Chen, Y. Fang, J. Zhang, S. Gao, X. W. Lou, *Angew. Chem. Int. Ed. Engl.* **2019**, *58*, 2675.
- [14] Y. Liu, Y. Fang, Z. Zhao, C. Yuan, X. W. Lou, *Adv. Energy Mater.* **2019**, *9*, 1803052.
- [15] Y. Fang, D. Luan, Y. Chen, S. Gao, X. W. Lou, *Angew. Chem. Int. Ed. Engl.* **2020**, *59*, 2644.
- [16] Y. Fang, D. Luan, Y. Chen, S. Gao, X. W. Lou, *Angew. Chem. Int. Ed. Engl.* **2020**, *59*, 7178.
- [17] L. Kong, C. Yan, J.-Q. Huang, M.-Q. Zhao, M.-M. Titirici, R. Xiang, Q. Zhang, *Energy Environ. Mater.* **2018**, *1*, 100.
- [18] M. Mon, R. Bruno, J. Ferrando-Soria, D. Armentano, E. Pardo, *J. Mater. Chem. A* **2018**, *6*, 4912.
- [19] X. F. Lu, L. Yu, X. W. Lou, *Sci. Adv.* **2019**, *5*, eaav6009.
- [20] J. Zhang, L. Yu, Y. Chen, X. F. Lu, S. Gao, X. W. Lou, *Adv. Mater.* **2020**, *32*, 1906432.
- [21] L. Zhang, H. B. Wu, Y. Yan, X. Wang, X. W. Lou, *Energy Environ. Sci.* **2014**, *7*, 3302.
- [22] Y. M. Chen, Z. Li, X. W. Lou, *Angew. Chem. Int. Ed. Engl.* **2015**, *54*, 10521.
- [23] X.-Y. Yu, L. Yu, X. W. D. Lou, *Adv. Energy Mater.* **2016**, *6*, 1501333.
- [24] X. Y. Yu, L. Yu, B. H. Wu, X. W. Lou, *Angew. Chem. Int. Ed. Engl.* **2015**, *54*, 5331.
- [25] L. Zhang, L. Zhou, H. B. Wu, R. Xu, X. W. Lou, *Angew. Chem. Int. Ed. Engl.* **2012**, *51*, 7267.
- [26] L. Yu, L. Zhang, H. B. Wu, X. W. Lou, *Angew. Chem. Int. Ed. Engl.* **2014**, *53*, 3711.
- [27] L. F. Shen, L. Yu, H. B. Wu, X. Y. Yu, X. G. Zhang, X. W. Lou, *Nat. Commun.* **2015**, *6*, 6694.
- [28] H. Hu, L. Han, M. Z. Yu, Z. Y. Wang, X. W. Lou, *Energy Environ. Sci.* **2016**, *9*, 107.
- [29] L. F. Shen, L. Yu, X. Y. Yu, X. G. Zhang, X. W. Lou, *Angew. Chem. Int. Ed. Engl.* **2015**, *54*, 1868.
- [30] H. C. Chen, J. J. Jiang, Y. D. Zhao, L. Zhang, D. Q. Guo, D. D. Xia, *J. Mater. Chem. A* **2015**, *3*, 428.
- [31] R. Li, S. Wang, Z. Huang, F. Lu, T. He, *J. Power Sources* **2016**, *312*, 156.

- [32] X. Y. Yu, X. W. David Lou, *Adv. Energy Mater.* **2018**, 8, 1701592.
- [33] L. Yu, X. Y. Yu, X. W. D. Lou, *Adv. Mater.* **2018**, 30, e1800939.
- [34] J. Nai, X. W. D. Lou, *Adv. Mater.* **2018**, e1706825.
- [35] G. Q. Zhang, X. W. Lou, *Angew. Chem. Int. Ed. Engl.* **2014**, 53, 9041.
- [36] J. B. Fei, Y. Cui, X. H. Yan, W. Qi, Y. Yang, K. W. Wang, Q. He, J. B. Li, *Adv. Mater.* **2008**, 20, 452.
- [37] S. Chen, M. Xue, Y. Li, Y. Pan, L. Zhu, S. Qiu, *J. Mater. Chem. A* **2015**, 3, 20145.